

## Effects of Wave Coherence on Longshore Variability of Nearshore Wave Processes



### Key Points:

- Wave coherence results in stationary interference in the wavefield leading to longshore variation of wave processes
- A new wavemaker is proposed which either eliminates the wave coherence or limits the number of coherent waves to a controlled number
- Longshore variations of nearshore wave processes in a longshore uniform domain increase as the number of coherent waves increases

### Correspondence to:

Q. Chen,  
[q.chen@northeastern.edu](mailto:q.chen@northeastern.edu)

### Citation:

Salatin, R., Chen, Q., Bak, A. S., Shi, F., & Brandt, S. R. (2021). Effects of wave coherence on longshore variability of nearshore wave processes. *Journal of Geophysical Research: Oceans*, 126, e2021JC017641. <https://doi.org/10.1029/2021JC017641>

Received 9 JUN 2021  
Accepted 12 OCT 2021

Reza Salatin<sup>1</sup> , Qin Chen<sup>1,2</sup> , A. Spicer Bak<sup>3</sup> , Fengyan Shi<sup>4</sup> , and Steven R. Brandt<sup>5</sup> 

<sup>1</sup>Department of Civil and Environmental Engineering, Northeastern University, Boston, MA, USA, <sup>2</sup>Department of Marine and Environmental Sciences, Northeastern University, Boston, MA, USA, <sup>3</sup>Coastal and Hydraulics Laboratory, US Army Engineer Research and Development Center, Duck, NC, USA, <sup>4</sup>Center for Applied Coastal Research, University of Delaware, Newark, DE, USA, <sup>5</sup>Center for Computation and Technology, Louisiana State University, Baton Rouge, LA, USA

**Abstract** Coherent waves are pairs of waves having identical frequency and waveform with constant phase difference leading to a stationary wave interference in the wavefield of phase-resolving wave models. The resulting stationary interference due to the presence of coherent water waves results in the longshore variation of the wave height in longshore uniform topography. Consequently, this variation affects the radiation stress throughout the domain and leads to the longshore variation in mean water level, mean current field, shear wave amplitude, wave setup, and wave runup. Here, we have developed a new method of wave energy spectrum discretization for the phase-resolving wave models like FUNWAVE-TVD, which either eliminates the coherent waves at the offshore boundary condition or limits them to a controlled number. Then, effects of the coherent waves on some nearshore wave processes are probed using both a flat bottom case as well as a longshore uniform sloping beach. The results shed light on the effects of wave coherence on the nearshore wave processes and demonstrate the usefulness of the newly developed wavemaker as a tool for the scientific community to further assess the hydrodynamics in nearshore environments.

**Plain Language Summary** It is well known that two wave trains having identical wave frequency and different wave angles result in alongshore non-uniformity of the wave field. These waves are called coherent waves that can affect nearshore wave processes, leading to alongshore variations in wave height, mean water level, and surfzone currents on an alongshore uniform beach. However, quantitative understanding of such effects under field conditions is rather limited. In this study, we develop a new method to generate directional random wave fields with various degrees of wave coherence in a phase-resolving Boussinesq wave model, which either eliminates the coherent waves at the offshore boundary condition or limits them to a controlled number. Then, effects of wave interference on nearshore wave processes are probed using numerical experiments on a flat bottom and an alongshore uniform barred beach. The results shed light on the role coherent waves play in alongshore variations of wave setup, wave runup, longshore currents, and rip currents. The new method can be implemented into other phase-resolving wave models for nearshore processes to quantify the effects of wave coherence on surfzone hydrodynamics and morphodynamics.

## 1. Introduction

Since Young's (1802) double-slit experiment with optical waves, wave coherence has been studied in various scientific fields including quantum mechanics and engineering. Wave coherence happens when two intersecting waves have identical wave frequency, waveform, and constant phase difference and result in a stationary wave interference in the wavefield. Despite the importance of the subject in various scientific fields, it has not been studied broadly for the water waves. In one of the earliest studies of coherent waves, Dalrymple (1975) investigated the longshore variation of the mean water level as well as the wave height and wave-induced circulation due to the existence of intersecting waves with equal frequencies. He showed that alongshore variation of wave height due to the presence of two coherent waves results in nodal and anti-nodal points alongshore, and rip currents are formed at nodal lines with zero wave height. Following his work, Z. Wei and Dalrymple (2017) carried out numerical experiments with the Lagrangian-based smooth particle hydrodynamics (SPH) model using two intersecting waves of the same period and confirmed the

© 2021. The Authors.

This is an open access article under the terms of the [Creative Commons Attribution-NonCommercial-NoDerivs](https://creativecommons.org/licenses/by-nc-nd/4.0/) License, which permits use and distribution in any medium, provided the original work is properly cited, the use is non-commercial and no modifications or adaptations are made.

generation of rip currents and undertow by short-crested wave breaking. Dalrymple and Lanan (1976) generated waves with a wavemaker and let some of the waves reflect from a vertical wall. Thus, they could generate intersecting waves near the beach and showed that rip currents generated by coherent interferences result in beach cusps. Furthermore, they categorized reflection from vertical walls and cliffs or refraction and diffraction around shoals and canyons as natural sources of wave intersection which can lead to coherent interference. For these scattered waves to produce coherent interference, though, the medium variations, like currents and topography, should be of the same order as the coherent length scale of the wave field. Because large medium variations exist in coastal and nearshore areas and swells have long coherent length scales, coherent wave interference is most likely to occur in the swell band (Smit et al., 2015a). Smit et al. (2016) also investigated the longshore variations of the nearshore wavefield through a field study by remote sensing techniques, which were very useful in understanding the wave coherence in the field where the pressure sensor cannot record the data for capturing the wave coherence.

While the above-mentioned studies were focused on perfectly coherent waves, rip currents and other along-shore varying wave processes can also occur when waves with close frequencies intersect. The former results in stationary rip currents, while the latter generates transient rip currents moving alongshore like a wave train (Dalrymple, 1975). For example, J. Choi et al. (2009, 2015) linked the longshore variation of wave height to the intersecting directional waves, which subsequently complicates the mixing process due to the fluctuations of the longshore and rip currents in the nearshore. In a recent study, J. Choi and Roh (2021) also confirmed the formation of transient rip currents in the node regions of a wavefield (Dalrymple, 1975). While these transient rip currents generated by short-crested waves with or without the presence of coherent waves can happen in shorter time scales, the focus of this study is on the perfectly coherent waves and resulting stationary rip currents.

Despite the significant effects of wave coherence on nearshore wave processes, phase-averaged models based on wave action balance are usually incapable of simulating the effects of the coherent interferences generated by bathymetric features. Considerable effort has been devoted to solving this problem in the literature. Janssen et al. (2008) derived a stochastic model for the linear and nonlinear interaction of directional waves over a two-dimensional topography accounting for wide-angle refraction, diffraction, and quadratic nonlinear coupling. Smit and Janssen (2013) and Smit et al. (2015a) introduced a new transport equation incorporating the coherent interference effects on the wave statistics in third-generation phase-averaged wave models. Later, Smit et al. (2015b) improved their previous model with the introduction of a source term to account for the depth-induced wave breaking. Though Smit and Janssen (2013) successfully modeled heterogeneous wave statistics, the wave field remained strictly Gaussian since the model assumed linear wave dynamics. Thus, Smit and Janssen (2016) proposed a new bispectral evolution equation taking non-Gaussian wave statistics in shallow water into account. Recently, Akrish et al. (2020) extended the capabilities of the model to consider the wave-current interaction.

Phase-resolving models, on the other hand, are capable of resolving wave coherence. However, in phase-resolving models like FUNWAVE-TVD (Chawla & Kirby, 2000; Chen, Dalrymple et al., 1999; Chen et al., 2000; Shi et al., 2012), wave coherence is either produced by the bathymetric features in the domain or at the offshore boundary due to the wave energy discretization techniques introduced by G. Wei et al. (1999). Since the latter may result in artificial alongshore variation of nearshore processes, efforts have been made to eliminate this problem by increasing the discretization resolution both in direction and frequency (Goda, 2010; Suh & Dalrymple, 1993). Moreover, single summation methods for the discretization of an input spectrum were used by Miles and Funke (1989), Van Dongeren et al. (2003), Johnson and Pattiaratchi (2006), and Rijnsdorp et al. (2015). In this study, a new single summation method is proposed to control the longshore variation of the wave processes due to the presence of coherent waves generated by the offshore boundary conditions. The newly proposed wavemaker discretizes the input energy spectrum in finer frequency bins, each having only a single directional bin. Therefore, no coherent waves are generated by the wavemaker. Furthermore, a limited number of waves can be moved from their original frequencies to other frequencies to form groups of coherent waves in the domain if desired. Thus, the effects of different levels of wave coherence on the nearshore wave hydrodynamics can be assessed. The new method is a generalized form of the default wavemaker in FUNWAVE-TVD, which is capable of producing a wavefield with varying degrees of wave coherence. This feature is useful for phase-resolving wave models beyond FUNWAVE-TVD.

This paper is organized as follows: In Section 2, a new wavemaker with varying levels of wave coherence is formulated. In Section 3, several numerical experiments are carried out to confirm the results of the new wavemaker and to investigate the effects of the coherent waves on the wave height distributions over a flat bottom. In Section 4, a more realistic case is analyzed and the effects of the coherent waves on the wave height, mean current field, vorticity field, wave setup, and wave runup are assessed for a case with obliquely incident waves. In Section 5, the findings are discussed and in Section 6, a summary is given.

## 2. Wavemaker Formulation

FUNWAVE-TVD (Shi et al., 2012) is a phase-resolving wave (Gobbi et al., 2000) and current (Chen et al., 2003) model based on the fully nonlinear Boussinesq equations which can simulate random directional waves (Chen et al., 2003; Chen, 2006; Kennedy et al., 2001; G. Wei et al., 1999). In Boussinesq wave models, the wavemaker is a longshore strip with a cross-shore width of  $W$  placed close to the offshore boundary of the domain for generating directional waves. To generate the waves in Boussinesq models, a source function is added to the mass conservation equation.

$$\eta_t + h \nabla \cdot \mathbf{u} + \alpha_1 h^3 \nabla^2 (\nabla \cdot \mathbf{u}) = C(x, y, t) \quad (1)$$

where  $\eta$  is the free surface elevation,  $t$  is time,  $h$  is water depth,  $\mathbf{u}$  is the velocity vector, and  $\alpha = -0.39$  and  $\alpha_1 = \alpha + 1/3$ . Moreover,  $C$  is the source term for the mass equation and can be written in the following form

$$C(x, y, t) = \exp(-\beta x^2) F(y, t) \quad (2)$$

where  $x$  is the cross-shore distance from the centroid of the wavemaker, and  $\beta$  is a free parameter describing the source width as determined below

$$\beta = \frac{80}{(\delta L)^2} \quad (3)$$

in which,  $\delta$  is the nondimensional wavemaker width with a typical value of 0.3–0.5, and  $L$  is the wavelength for a representative wave having peak frequency and main propagation direction. Furthermore,  $F$  is the time series of the source function and is defined in the following sections for each wavemaker.

While the source function formulation for the default wavemaker is provided in the appendix, the new wavemaker without coherent waves and a controlled number of coherent waves are formulated in this section. It should be mentioned that the input wave energy spectrum is discretized in both frequency and directional axes, thus, generating discretized wave energy packets associated with each frequency and directional component. The wavemaker, thus, generates single waves, which will be called wave components hereafter, with the discretized wave energy packets. Therefore, the irregular wavefield comprises the super-positioned single wave components generated by the wavemaker.

### 2.1. New Wavemaker Without Coherent Waves

In FUNWAVE-TVD's default wavemaker, each frequency component of the discretized energy spectrum accommodates several coherent wave components. In the proposed wavemaker without coherent waves, though, each frequency component has one and only one wave component. Therefore, the number of frequency components is equal to the directional components and a single index is sufficient to represent each wave component in the discretized spectrum. The time series of the source function for the new wavemaker can be formulated as

$$F(y, t) = \sum_{i=1}^N D_i \cos(\omega_i t - k_i \cos(\theta_i) y + \phi_i) \quad (4)$$

where subscript  $i$  corresponds to the wave component index and  $D_i$  is source function amplitude for each wave component, which is a slightly modified version of the default wavemaker's formulation (G. Wei et al., 1999). The source function amplitude is formulated as

$$D_i = \frac{2a_i (\omega_i^2 - \alpha_1 g k_i^4 h^3) \cos(\theta_i)}{\omega_i I_1 k_i (1 - \alpha k_i^2 h^2)} \quad (5)$$

with the wave amplitude for each wave component as

$$a_i = \sqrt{\frac{E_i \bar{A}_i H_{mo}^2 df}{8 \sum_i E_i df}} \quad (6)$$

and directional weight of each wave component as

$$A_i = \frac{1}{2\pi} + \frac{1}{\pi} \sum_{k_n=1}^{N_s} \left( e^{-0.5(k_n * \sigma_\theta)^2} \right) \cos(k_n * (\theta_i - \theta_{mean})) \quad (7)$$

which is normalized differently from the default wavemaker as illustrated in Equation 8.

$$\bar{A}_i = \frac{A_i * \sum_{i=1}^N (E_i * df)}{\sum_{i=1}^N (A_i * E_i * df)} \quad (8)$$

It should be noted that wave energy spectrum discretization can be carried out in various ways. As mentioned in the introduction, single summation methods were proposed and used before. Miles and Funke (1989) used a spiral method in which no two wave components have equal frequencies. However, their discretized spectrum is biased toward higher frequencies at one side and is asymmetric. This problem, though, might be alleviated with a higher resolution of frequency discretization. Their method was later used by Van Dongeren et al. (2003) as well. Johnson and Pattiaratchi (2006) used a similar method by introducing spectral bins as pairs with opposite directions, but there was a standing wave problem in their method. Rijnsdorp et al. (2015) used a method similar to Miles and Funke (1989), however, the wave directions were randomly chosen using a cosine probability density function centered at a mean wave angle varying over different frequencies. While this method would work for an analytic wave energy spectrum, measured bimodal wave spectra might lose some of their energy because most of the wave components are concentrated in a specific directional range around the mean wave angle. The proposed single summation method is a generalized form of the default method by introducing varying coherency levels in Section 2.2. Therefore, this study informs the model users about the implications of using the default method without considering the coherency level and gives them an option to either eliminate the wave coherency in their simulations or bring it to a controlled level by the proposed wavemaker. Moreover, this method is not restricted to FUNWAVE-TVD and can be employed by other phase-resolving wave models that use the single or double summation methods in their wavemakers.

## 2.2. New Wavemaker With Coherent Waves

The inclusion of the coherent waves in the previous formulation is outlined here. The only difference is that some wave frequencies, which are named as host frequencies and originally include the wave components propagating in the mean direction in the new wavemaker with no wave coherence, will also include the wave components displaced from the adjacent frequencies and will form groups of coherent waves. Since the percentage of the coherent waves in the new wavemaker is decided by the user, this part of the program operates when the percentage is greater than zero. Therefore, to introduce the coherent waves into the offshore boundary condition, a portion of the original wave components are selected to be displaced to the host frequencies as follows

$$N_c = \frac{\alpha_c}{100} N \quad (9)$$

where  $\alpha_c$  is the percentage of the original waves considered as coherent waves given to the model as an input and can have a value ranging from 0 to 100. Thus, a range of wave coherence from wave components having no coherent waves ( $\alpha_c = 0$ ) to multiple coherent waves at all frequencies ( $\alpha_c = 100$ ) like the default wavemaker can be generated. Additionally,  $N$  is the number of original wave components with distinct frequencies in the proposed wavemaker and  $N_c$  is the total number of coherent waves. After determining the number of coherent waves, frequencies of these waves are randomly selected from the pool of the existing wave frequencies as follows

$$f_{C_k} = f(P_k \times N), P \sim U(0,1) \quad (10)$$

where  $P$  is a random real number selected from a uniform distribution ( $U$ ), and when multiplied by the number of the wave components, determines the index number of the wave frequencies chosen for generating the coherent waves. Moreover,  $f$  is the pool of the original wave frequencies and  $f_{C_k}$  is the  $k$ th randomly selected wave frequency. After randomly selecting the wave components, their frequency is replaced with



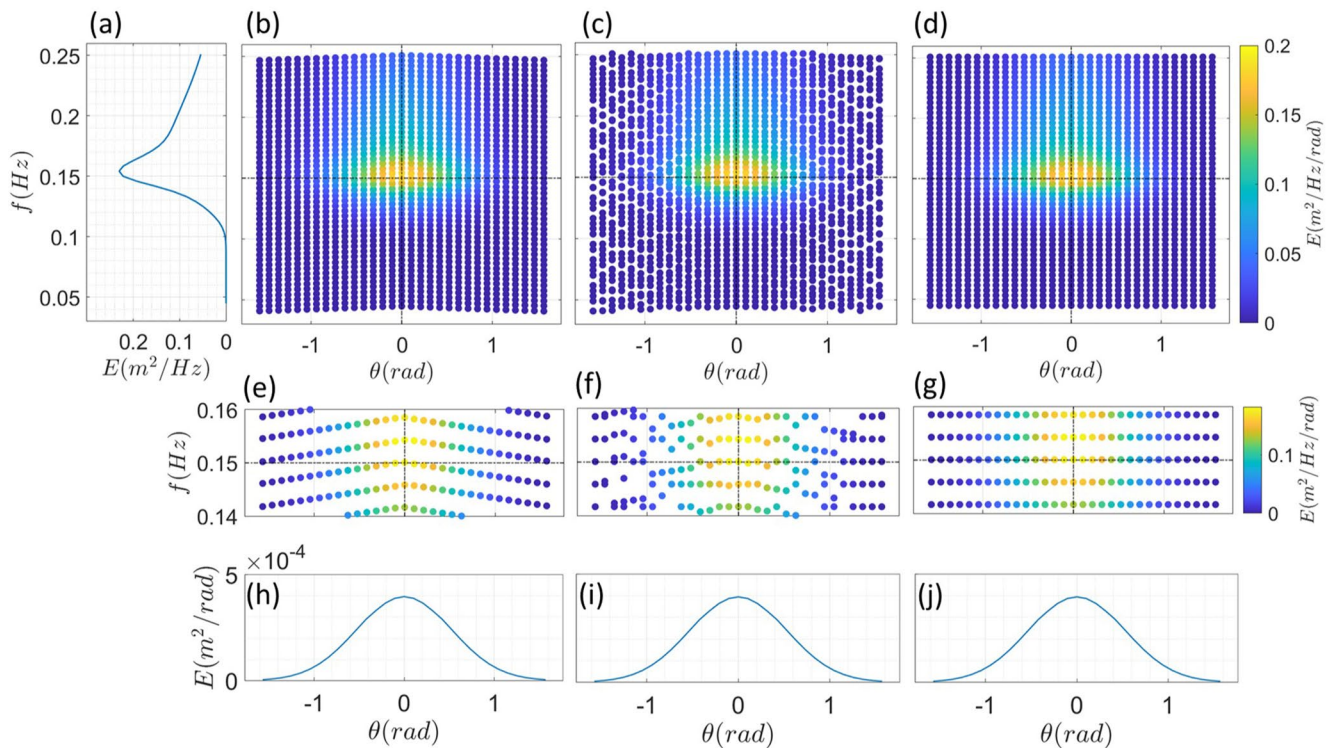


**Figure 1.** Energy spectra for the FUNWAVE-TVD directional wavemaker. (a) The spectra integrated through the directional axis, (b) discretized spectrum with 0% wave coherence, (c) with 50% wave coherence, and (d) with 100% wave coherence. (e–g) Enlarged view of the discretized spectra around the peak frequency and mean direction. (h–j) The integrated spectra through the frequency axes.

the frequency of the nearby host frequencies. After moving the wave components into their new frequencies, the wave energy of each wave component will be redistributed based on their new frequencies. Figure 1 demonstrates the energy spectra constructed by three levels of wave coherence: (b) 0% wave coherence, (c) 50% wave coherence, and (d) 100% wave coherence which is similar to the spectrum discretization in the default directional wavemaker. Moreover, enlarged views of the spectra are illustrated in the panels (e–g) for better illustration of the wave component distribution. The integration of the spectra in the directional and frequency axes are shown in panel (a) and panels (h–j), respectively. While the wave energy spectra with 0% and 100% coherence are fully discussed in the two following sections, the 50% coherence is postponed to the discussion section.

### 3. Numerical Experiments on a Flat Bottom

#### 3.1. Model Setup

To assess the performance of the wavemaker, four simple flat bottom scenarios are prepared. The generated random directional waves have a peak frequency and significant wave height of 0.15 Hz and 0.5 m, respectively. Thus, with a constant water depth of 9.6 m for the domain, the wavelength of the waves with the peak period is about 55.31 m. The model extends both in  $X$  and  $Y$  directions about 9 wavelengths with the sponge layers covering about 1.8 wavelengths from each side which is an acceptable range according to Chen, Madsen, and Basco (1999). The wavemaker is positioned at 2.7 wavelengths from the left boundary and 0.9 wavelengths from the closest sponge layer. Furthermore, periodic boundary conditions are applied at the lateral boundaries to avoid the reflection of the waves back into the domain.

As shown in Table 1, four cases are analyzed to investigate the performance of the wavemaker in different frequency and directional spreading. Each case is assigned with an ID, in which letters B, N, F, and D refer to broad, narrow, frequency spreading, and directional spreading, respectively. While the three main components of the water depth, zero moment wave height, and peak wave period are the same in four cases,

**Table 1**  
Directional Spectrum Parameters for Four Different Scenarios

Directional spreading	Frequency band	ID	$\gamma_{\text{TMA}}$	$\sigma_{\theta}$ (deg)
Broad	Broad	BDBF	2	30
	Narrow	BDNF	20	30
Narrow	Broad	NDBF	2	10
	Narrow	NDNF	20	10

the TMA parameter ( $\gamma_{\text{TMA}}$ ), as well as the directional spectrum parameter ( $\sigma_{\theta}$ ) for G. Wei et al. (1999) irregular wavemaker constitute four different scenarios for the analyses. For the default wavemaker, energy spectra are evenly discretized into  $N = 50$  and  $M = 31$  components in frequency and directional axes, respectively. The number of frequency bins is slightly larger than the default value of FUNWAVE-TVD, which is 45. The number of directional bins is also larger than the default value of 24 in FUNWAVE-TVD. For the new wavemaker, the number of wave components with distinct frequencies is  $N \times M = 1,550$ .

The three-dimensional views of the energy spectra for four different scenarios are illustrated in Figure 2. The frequency range is from 0.04 to 0.25 Hz and the wave direction is in the range of  $-90^{\circ}$  to  $90^{\circ}$ , with the mean direction of zero degrees. The  $\bar{k}h$  values for broad and narrow-banded spectra lie within the recommended ranges by Suanda and Feddersen (2015) to achieve sufficient accuracy for the model results.

The shortest wavelength in the domain is about 24.6 m and considering the grid resolution of 1 m in both horizontal and vertical directions, the ratio of the shortest wavelength to the grid size is approximately 25, which can assure the negligible numerical diffusion of the wave energy for the shortest waves. Wavemaker width parameter ( $\delta$ ) for G. Wei et al. (1999) irregular wavemaker is also 0.5, which with a characteristic wavelength of 55.31 m, the wavemaker width is about 13.8 m. The sponge layers, which cover both sides of the domain are a combination of L-D type (Larsen & Dancy, 1983) and friction type. The free parameters of the L-D type sponge are assigned as  $\alpha_s = 2$  and  $\gamma_s = 0.85$ . The value of  $\gamma_s$  is slightly less than the recommended value of  $\gamma_s = 0.88$ – $0.92$  by Chen, Madsen, and Basco (1999). However, since the L-D type sponge is problematic in long-term simulations, it is accompanied by the friction type sponge to minimize the generation of sawtooth noise within the domain. For the friction-type sponge layer, the value of  $C_{d_{\text{max}}} = 1$ . Additionally, the bottom friction coefficient for the whole domain is constant and equal to 0.002. The four cases were run for 1,350 peak wave periods with a CFL value of 0.3 and a total number of 12 wave gauges, as illustrated in Figure 3.

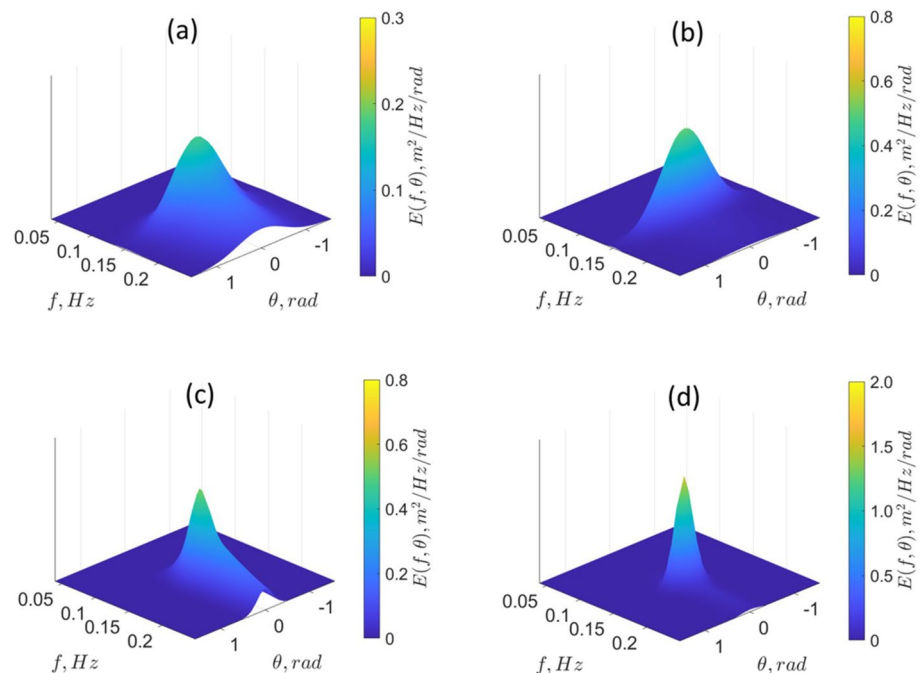


**Figure 2.** Three-dimensional view of the input energy spectra for (a) BDBF, (b) BDNF, (c) NDBF, and (d) NDNF scenarios.

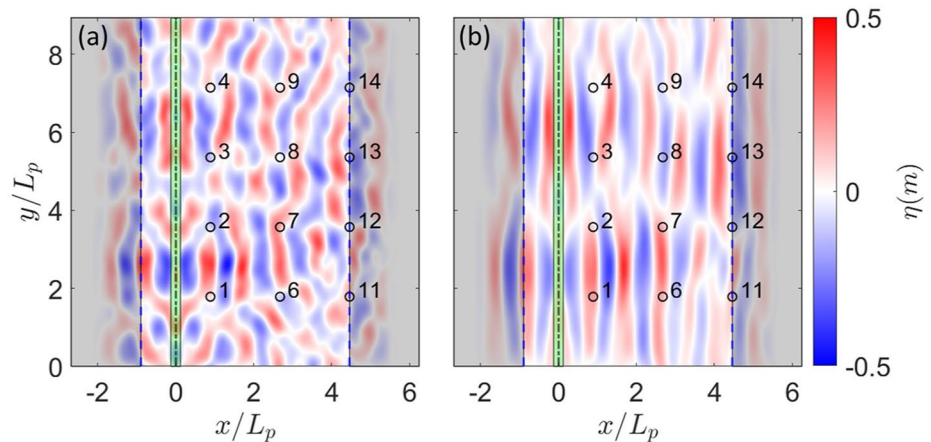


**Figure 3.** Surface elevation snapshot of the normally incident directional waves for (a) broad directional spreading and (b) narrow directional spreading with 12 wave gauges. The gray areas denote the sponge layers at both boundaries and the green strip and dotted line depict the wavemaker width and wavemaker line, respectively.

### 3.2. Model Results

The surface elevation snapshot at the end of the simulation is shown in Figure 3, illustrating the location of the 12 wave gauges with circles, sponge layers with the gray area, wavemaker line with the dash-dotted line, and wavemaker width by the green shaded area. The geometry of the domain is nondimensionalized with the wavelength corresponding to the peak wave period. Short-crested waves are visible in the broad directional spreading case, which is due to the higher energy levels of the waves not propagating in the mean direction. In the narrow directional spreading case, which most resembles the unidirectional waves because of the lower energy levels of the waves not propagating in the mean direction, the waves demonstrate longer crest lengths.

In FUNWAVE-TVD, root mean square wave height ( $H_{rms}$ ) calculation is carried out using the zero-crossing of the surface elevation at each grid point over a certain period. In the present study, the zero-crossing is performed over 1,080 peak periods, with 270 peak periods for the spin-off at the start of the simulation, thus, totaling 1,350 peak periods for the whole simulation. Allowing sufficient time for the wave height calculation is important since the longshore variability in wave height originates from two sources. First, the interference between the waves with very close frequencies, which will fade away with time. Second, the phase interference between the coherent waves having equal frequencies, which is independent of time and results in a wave height distribution with permanent spatial variation.

The  $H_{rms}$  distributions over the domain for the default and new wavemaker in four different scenarios are demonstrated in Figure 4. For the scenarios using the default wavemaker, which includes numerous coherent waves, differences in the wave height distribution patterns are notable. The broad frequency spreading results in smoother wave height variation than the narrow frequency spreading. This can happen due to the accumulation of the energy at fewer frequency bins in narrow frequency bands and thus, can intensify the wave interference of the coherent waves with the adjacent frequencies. For the broad frequency band, though, since each frequency has lower energy due to a more uniform energy distribution among the frequencies, the wave interference is not as intense as in the previous case. Moreover, the wave height variation pattern is more complex in broad directional spreading than the narrow directional spreading as illustrated in Figure 4. The reason can be sought in the energy levels of the wave components not propagating in the mean direction. In broad directional spreading scenarios using the default wavemaker, these wave components receive higher energy levels compared to the narrow directional spreading cases, and thus, the wave-wave interference of the coherent waves and the resultant wave height variation is more complex. In summary, for the default wavemaker, storing most of the energy at some limited number of frequencies and then distributing it in roughly equal proportions among its coherent waves will intensify the wave interference, and thus the longshore variation of the wave height will increase. For the cases with the newly proposed wavemaker, where no coherent waves exist, all four scenarios result in longshore, as well as

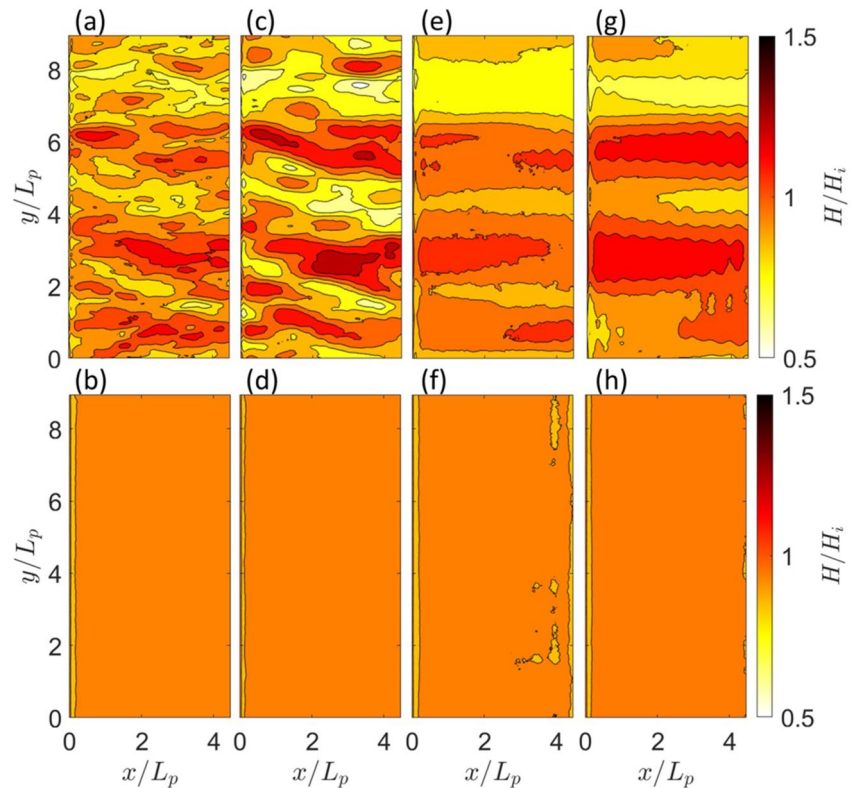


**Figure 4.** Nondimensionalized  $H_{rms}$  distribution (1,080 peak periods) over the domain for (a and b) BDBF, (c and d) BDNF, (e and f) NDBF, and (g and h) NDNF scenarios. Top subfigures (a, c, e, and g) use the default wavemaker, while bottom subfigures (b, d, f, and h) use the new wavemaker with 0%-coherence. Wave height is nondimensionalized with the input wave height and both axes are nondimensionalized with the wavelength corresponding to the peak period.

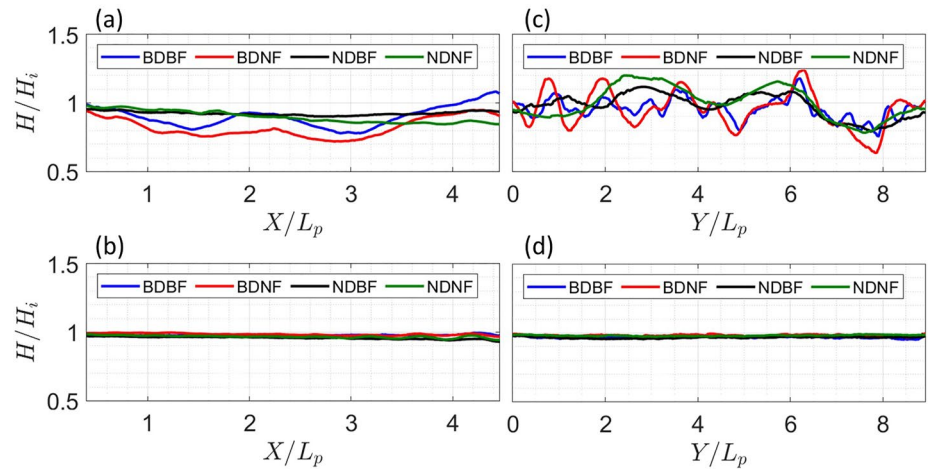
cross-shore uniform wave height distributions. Some irregularities are present in the NDBF scenario for the newly proposed wavemaker, which is due to the wave reflection from the sponge layers.

Figure 5 illustrates the longshore and cross-shore transects of the nondimensionalized  $H_{rms}$  distributions for all scenarios. The cross-shore transect is at the middle of the domain and the longshore transect is one wavelength away from the wavemaker. The new wavemaker, while generating the target wave height for all scenarios, can maintain alongshore uniform wave height as well. A closer look at the cross-shore transects of the new wavemaker reveals that the NDBF scenario has the most diffusion, which can be due to the damping of the shortest waves. Moreover, increased variation at the right boundary of the panel (b) is due to the partial reflection from the sponge layers.

The energy spectra of the wave gauges 2 and 7 for the BDBF case are obtained by the DIWASP (Johnson, 2002) MATLAB® toolbox and are illustrated in Figure 6. The energy spectra from the analyses with default wavemaker illustrate high discontinuous peaks, which are the result of the interference of the coherent waves. To make a fair comparison, the color bar and vertical axes are kept constant in both wavemaker and thus, the peaks of the default wavemaker spectra have surpassed the axial limits. The energy spectra of the scenarios using the new wavemaker, though, have the most similarity to the input wave energy spectrum. However, a slight increase in the energy level at the peak frequency is seen at wave gauge 7 (Figure 6d).

In the end, it can be concluded that the new wavemaker, in the absence of the coherent waves can generate the longshore uniform target wave height. Moreover, a comparison of the wave energy spectra showed that the new wavemaker can regenerate the input wave spectrum at some distance away from the offshore boundary. While generating various degrees of wave coherence in a controlled manner, the new wavemaker may lower the calculation speed because of the increased number of wave frequencies. This problem is partly solved by performing optimization on the source code of the model to avoid redundant operations.





**Figure 5.** Nondimensionalized  $H_{rms}$  transects in (a and b) cross-shore, and in (c and d) longshore directions for the default wavemaker and new wavemaker with 0% wave coherence, respectively. Four lines refer to four different scenarios. Wave height is nondimensionalized with the input wave height and both axes are nondimensionalized with a wavelength corresponding to the peak period.

Numerical stability is not affected by the new wavemaker. Thus, by confirming the ability of the new wavemaker in generating the target wave height, it is applied to a scenario with the sloping topography to investigate the nearshore wave processes.

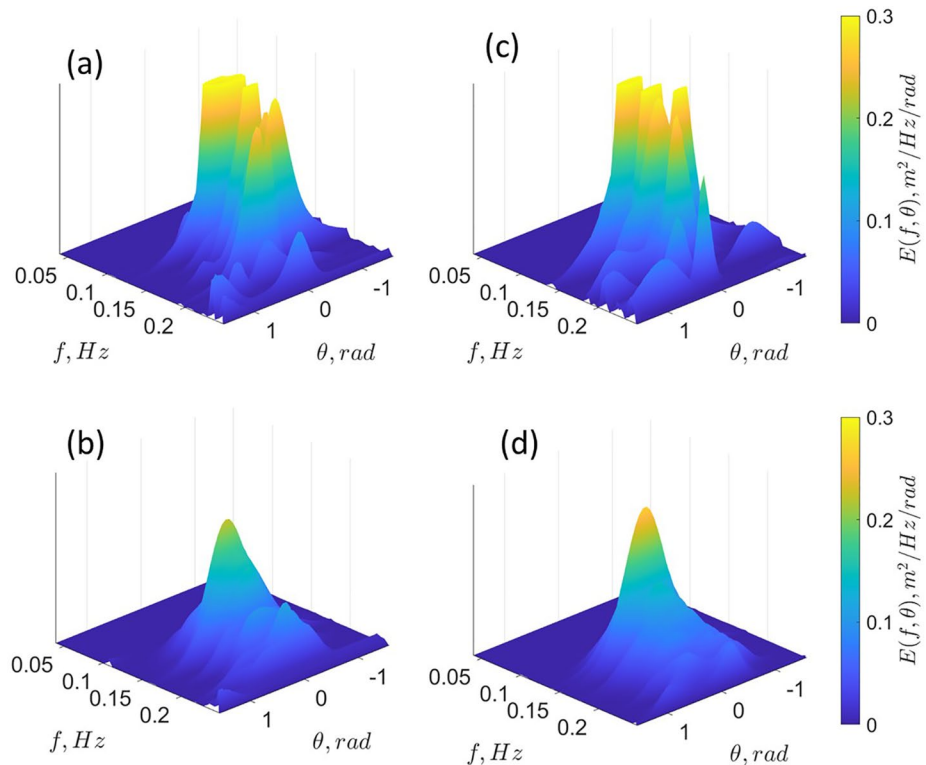


**Figure 6.** Three-dimensional spectra of the waves generated for the BDBF scenario by the default and new wavemaker for (a and b) WG2 and (c and d) WG7 for default and new wavemaker with 0% wave coherence, respectively.

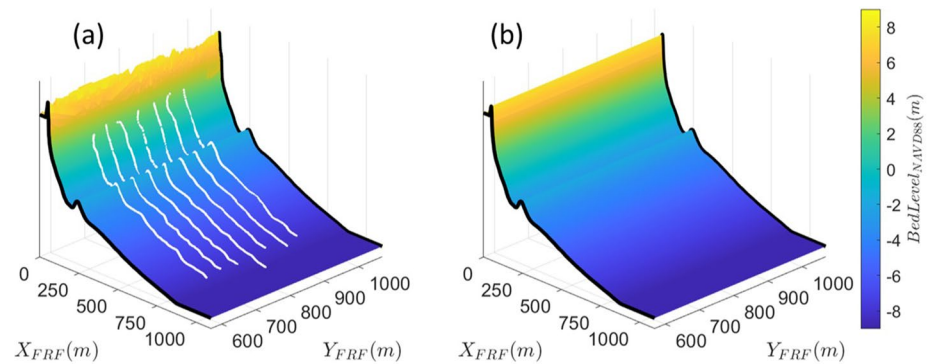


**Figure 7.** (a) Longshore varying, and (b) longshore averaged topography of the barred beach at Field Research Facility, Duck, NC. Seven parallel white lines in (a) represent the CRAB surveys, and the dune is modeled by the Dune Lidar data.

## 4. Numerical Experiments on a Sloping Beach

### 4.1. Model Setup

To investigate the effects of the offshore boundary conditions on the nearshore wave processes like the mean current field, vorticity field, wave setup, and wave runup, an idealized field setup using data from the Field Research Facility (FRF), Duck, NC is employed. As demonstrated in Figure 7, field topography is constructed by fusing two sets of field data. The dune part, which is shown by the rigged area in Figure 7a is constructed by the dune lidar data, which is surveyed in October 2019. The remaining part is modeled by the field data from the CRAB surveys on October 17, 2019 as shown by the white lines. Due to the limited coverage from the dune-based lidar, the data were mirrored in the alongshore direction, then the whole domain was alongshore averaged to eliminate the effects of the longshore varying topography on the wavefield and isolate the effects of the coherent waves on nearshore processes. The modeled area covers  $Y = 568\text{--}1,068$  m in the longshore direction and  $X = 0\text{--}1,100$  m in the cross-shore direction in the FRF coordinates, with a 1.0 m grid size in both directions.

This study employs the bulk statistics of wave height, wave period, and mean water level of the 8m Array (Long & Oltman-Shay, 1991) from 00:00 to 01:00 EST, October 13, 2019, to generate the analytic spectra with the TMA and wrapped normal distribution functions. The frequency band domain extends from 0.04 to 0.25 Hz and the directional domain cover from  $-90$  to  $90^\circ$ . The TMA spectrum coefficient is  $\gamma_{\text{TMA}} = 2$  and the directional spreading parameter is  $\sigma_\theta = 30^\circ$ . Therefore, the input energy spectrum will be similar to the BDBF case in the previous section. The energy spectrum in the default wavemaker is discretized into 31 directional (spaced  $6^\circ$  apart) and 50 frequency components, resulting in a total of 1,550 wave components. As mentioned before, these values are close to FUNWAVE-TVD's default frequency and directional bin values. In the new wavemaker, however, the energy spectrum is discretized into the same number of wave components in an arrow shape, and the highest energy is locked with the mean direction and peak frequency to ensure that a wave component with those characteristics is generated by the wavemaker. As illustrated in Table 2, one case is generated for the analyses with waves propagating in the mean direction obliquely incident to the shoreline. Moreover, the same scenario with normally incident waves is also analyzed with different levels of wave coherence, which will be discussed in Section 5. The water depth at the 8m Array is 8.8 m and the mean water level for the specified event is 0.8 m with respect to the NAVD88 datum. Therefore, the total water depth at the wavemaker location is 9.6 m. Generated irregular waves travel a short distance on the flat bottom before they start shoaling on the sloping beach. Moreover, the Ursell number ( $HL^2/h^3$ ) for

the cases illustrates the high nonlinearity of the generated waves. The three-dimensional view of the energy spectrum of the normally incident case and the contour plot of the energy spectra of both normally incident, as well as the obliquely incident cases are demonstrated in Figure 8.

Since the model is longshore uniform, the periodic boundary condition is used for the lateral boundaries. The wavemaker is also placed at

**Table 2**  
Input Wave Properties for Sloping Beach Case

$T_p$ (sec)	$H_{m0}$ (m)	$\gamma_{\text{TMA}}$	$\sigma_\theta$ (deg)	$h$ (m)	$\theta$ (deg)	$HL^2/h^3$	$a/h$
13.0	1.22	2	30	9.6	$0 \sim -15$	14.35	0.045

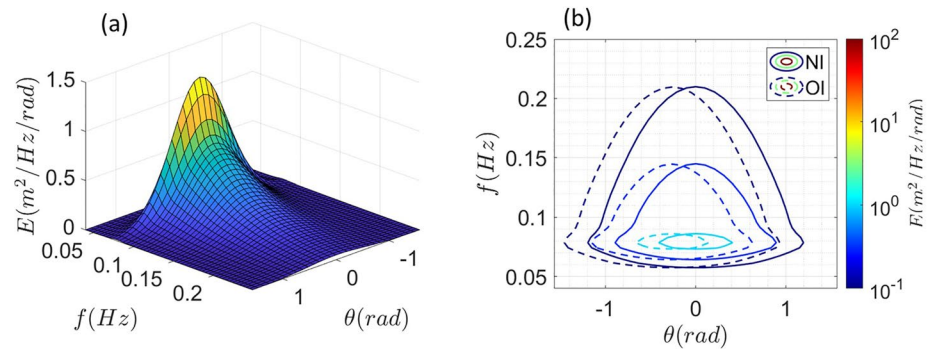


**Figure 8.** (a) Three-dimensional view of the energy spectrum for normally incident case and (b) contour plot of the energy spectra for normally incident and obliquely incident cases.

$X = 900$  m with the sponge layer covering the range of  $X = 950$ – $1,100$  meters to absorb the waves propagating offshore. The viscosity breaking method with the breaking parameters,  $C_1 = 0.45$  and  $C_2 = 0.35$  according to Y. Choi et al. (2018) is utilized and the CFL number of 0.5 is used for the analyses. The bottom friction is taken equal to 0.002 for the whole domain, as well. The simulation is carried out for 2.5 h, with the key processes, like wave height and mean current field, averaged over 2 h or 533 peak periods.

#### 4.2. Model Results

For the obliquely incident case, the cross-shore profiles of the  $H_{rms}$ , mean longshore current speed, the standard deviation of the instantaneous vorticity (shear wave amplitude) for 2 h of simulation, bottom elevation (NAVD88), and still water level are illustrated for both wavemakers in Figure 9. The figures show the wave processes in three different cross-shore locations, from which two are 50 meters away from the lateral boundaries and the other one is at the middle of the domain. In Figure 10a, these lines correspond to the longshore coordinates of wave gauges 36, 38, and 40.

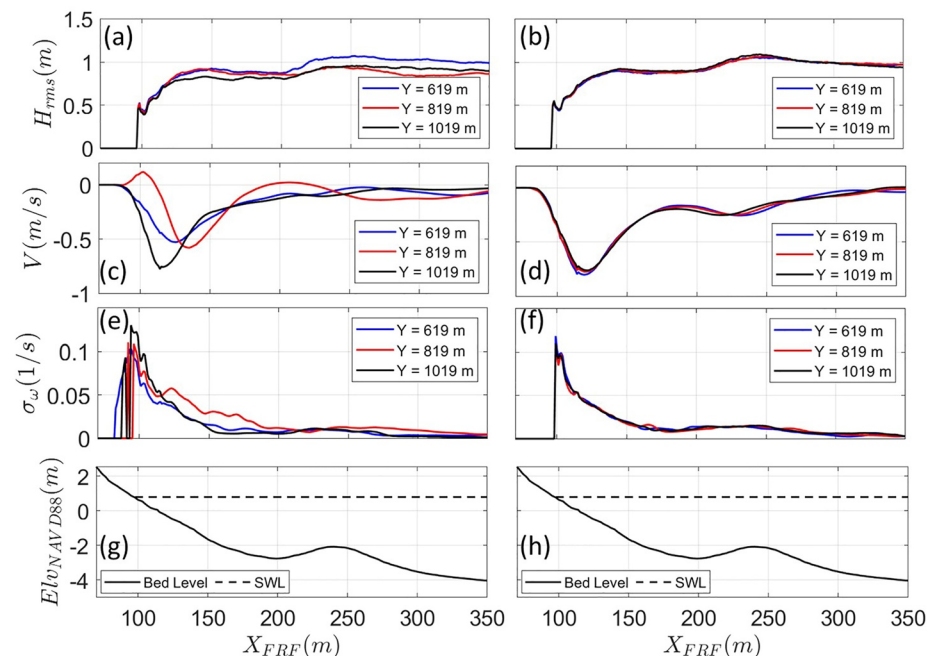


**Figure 9.** Cross-shore transects of (a–b)  $H_{rms}$ , (c–d) longshore current speed, (e–f) vorticity intensity, and (d–h) bed level with still water level for default wavemaker and new wavemaker with 0% wave coherence, respectively.

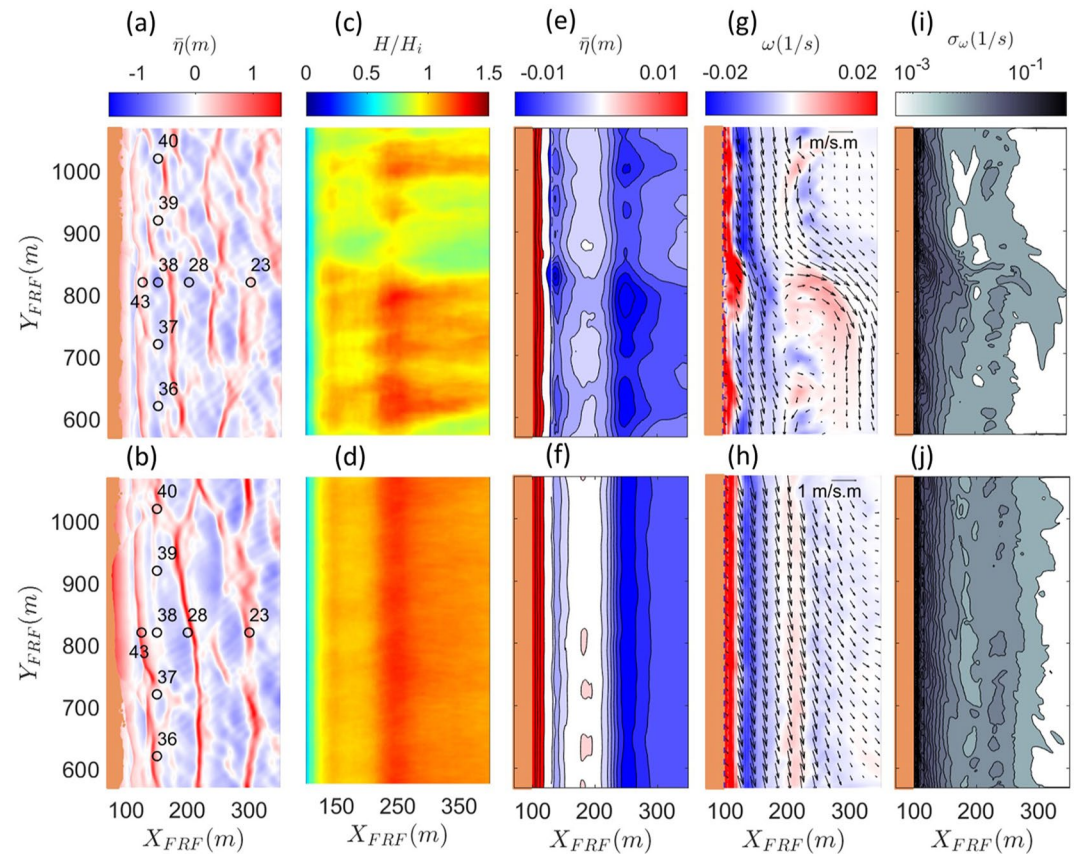


**Figure 10.** Spatial distributions of (a–b) instantaneous surface elevation, (c–d) nondimensionalized  $H_{rms}$ , (e–f) mean water level, (g–h) depth-integrated mean current field, and (i–j) vorticity intensity for default wavemaker and new wavemaker with 0% wave coherence, respectively.

For the default wavemaker, the effect of the coherent waves on the wave height is noticeable from Figure 9a. The cross-shore variations of the wave height are a mixed process containing the interference of the coherent waves as well as the wave shoaling and energy dissipation through wave breaking. Moreover, longshore variations of the wave height can also be observed as the differences between the wave height transects. The new wavemaker, though, has resulted in the longshore uniform wave height, and the bathymetry effects on the wave height variations across the domain including the wave shoaling and breaking can be observed in Figure 9b.

For the longshore current speed in the default wavemaker, the initial wave breaking above the sandbar has driven the longshore currents to gain speeds close to 15 cm/s in Figure 9c. However, secondary breaking which occurs close to the shoreline leads to the longshore current speed up to 75 cm/s at  $X = 120$  m. While three transects have different longshore current speeds, the one at  $Y = 1,019$  m is very similar to the longshore uniform current speed shown in Figure 9d for the new wavemaker. Thus, in using the default wavemaker of FUNWAVE-TVD, it is possible to select a random transect and still get rather reasonable results. Moreover, a change in direction of the longshore current at  $Y = 819$  m is observed in Figure 9c. High longshore gradients of wave height for the default wavemaker at this region can be observed from Figure 10c, resulting in the convergence of the feeder longshore currents and consequently, generation of the rip currents.

The location of the maximum longshore current speed is also affected by the coherent waves. As it can be seen from Figures 9c and 9d, for the default wavemaker, each transect has maximum longshore current speed at different cross-shore locations. Due to the interference of the coherent waves, the excess momentum flux throughout the longshore uniform domain is also longshore varying. This results in variations in the cross-shore location of the maximum longshore currents. The change in the cross-shore location and



direction of the maximum longshore current is very important. The presence of coherent waves can drive many morphological changes throughout the domain even when the bathymetry effects on the wave height are negligible. The vorticity intensity, which is calculated by the standard deviation of the instantaneous vorticity throughout the domain and represents the shear wave amplitude, demonstrates similar patterns as well. According to Figure 10i, in the default wavemaker, its value inside the sandbar trough is longshore non-uniform and is negligible around  $Y = 900$  m, where wave height is lower than the surrounding areas. Around  $Y = 819$  m, which is a nodal region, the shear wave amplitude increases, which illustrates the instabilities of the longshore current at that point and results in the formation of the rip currents (J. Choi & Roh, 2021). The new wavemaker, though, in the absence of coherent waves, shows longshore uniform wave height, mean current speed, and shear wave amplitude for the longshore uniform topography. However, transient eddies and rip currents still exist, as they are produced by the short-crested waves generated by the new wavemaker regardless of wave coherence. Due to higher water levels compared to other studies like Chen et al. (2003), a major portion of the wave breaking is delayed till the shoreline. This results in a maximum longshore current of about 75 cm/s and maximum shear wave amplitude of more than 0.1 1/s near the shoreline leaving the sandbar trough at a standstill condition.

Furthermore, the spatial distribution of the instantaneous surface elevation at the end of the simulation, nondimensionalized  $H_{rms}$ , mean water level, the depth-integrated mean current field with mean vorticity, and vorticity intensity are demonstrated in Figure 10. Apart from the longshore variations of the wave height and longshore currents which are discussed above, the formation of the rip currents at the middle of the domain and shifting the strong longshore currents to seaward direction can be observed from Figure 10. The location of the rip current coincides with the high gradients in the wave height and lower mean water level parts.

Effects of the coherent waves on the extreme runup values are also investigated in the current study. For that purpose, the instantaneous runup values are recorded alongshore for the whole simulation period of about 2.5 h. However, the initial 30 min of runup data are eliminated as the spin-off. The runup data is recorded alongshore using the mask property of the FUNWAVE-TVD, with a minimum depth of 10 cm and a sampling frequency of 4 Hz. The runup time series are analyzed by the time-domain (zero-crossing) and spectral-domain methods, as employed by Stockdon et al. (2006). Wave setup and 2% exceedance value of runup,  $R_{2\%}$ , are also obtained with the empirical equations according to Stockdon et al. (2006). A summary of both methods is provided in the appendix. Wave setup, significant swash height, and the extreme wave runup ( $R_{2\%}$ ) obtained by spectral and time domain analyses for both wavemaker with the obliquely incident wave angles are illustrated in Figures 11a–11f. Though the wave setup is dependent on the mean water level and wave height near the shoreline, significant swash height is found not to have a clear correlation with the nearshore wave processes such as wave height and mean water level. The empirical setup values, which are only dependent on the offshore wave height and wavelength, as well as the beach slope, are demonstrated in Figures 11a and 11b. Since the foreshore beach slope used in the empirical equations is acquired using the runup time series from numerical experiments, small longshore variations in empirical values can be observed. Empirical wave setup values in both cases are lower than the numerical values as illustrated in Figures 11a and 11b. However, empirical values are higher in significant swash heights according to Figures 11c and 11d. Overall, numerical values of  $R_{2\%}$  are lower than the empirical values for the default wavemaker and are very close to the empirical values in the new wavemaker with zero wave coherence as shown in Figures 11e and 11f. However, in both cases, the longshore variability can be observed which is mostly due to significant swash height.

The capability of the new wavemaker to generate realistic wave runup is further examined in Figures 11g and 11h, where the wave energy spectra from three wave gauges near the shoreline i.e., WG 36, 38, and 40, as illustrated in Figures 10a is compared against the runup energy spectra alongshore. The total water level (TWL) (aka runup) time series were analyzed to generate spectra for every cell in the alongshore direction of the domain. The envelope of variability for the TWL is calculated by OCEANLYZ (Karimpour & Chen, 2017) and is plotted in Figures 11g and 11h. The default wavemaker has a wider range of variability and smaller overall values when compared to spectra generated from the new wavemaker. This can also be observed from the  $R_{2\%}$  variations caused by the new wavemaker in Figures 11g and 11h. Moreover, according to Figures 11g and 11h, the variations in significant swash height in both wavemaker are mostly

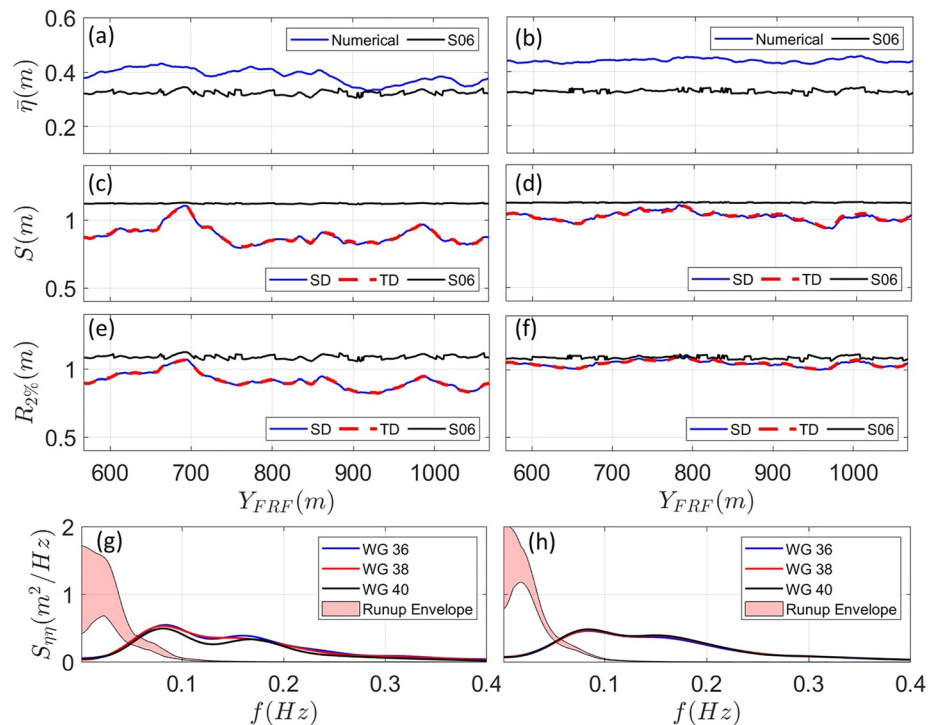


**Figure 11.** (a–b) Wave setup, (c–d) significant swash height, and (e–f) extreme wave runup values by spectral-domain analysis method (SD) and time-domain analysis method (TD) and Stockdon et al.'s (2006) empirical equations (S06) for the obliquely incident case. (g–h) Energy density spectra of surface elevation for three wave gauges as well as the longshore envelope of runup energy density. Left panels illustrate the results of the default wavemaker, and right panels demonstrate the results of the new wavemaker with 0% wave coherence.

due to the infragravity band and lower wave frequencies. The processes impacting alongshore variability of wave runup are not well understood. One of the reasons for lower runup values in the case of the default wavemaker could be the presence of strong stationary rip currents in the domain (Lerma et al., 2017). These currents could interact with the incoming waves and result in runup variations alongshore. The other reason can be the size of  $\Delta f$  values in the discretized spectrum. This value can affect nonlinear triad interactions and infragravity waves.

## 5. Discussion

Effects of the offshore boundary conditions with numerous coherent waves were assessed in two previous sections. Phase-resolving numerical models, including FUNWAVE-TVD, precisely discretize the energy spectra into frequency bins and then divide each frequency bin into several directional bins resulting in coherent wave components generated by the wavemaker. However, nature is random and the wave components from the discretized wave energy spectra in real-world conditions may not be well arrayed with equal frequencies. Furthermore, we showed that the default discretization of the wave energy spectra in FUNWAVE-TVD can result in considerable longshore fluctuations in wave processes like  $H_{rms}$ . This problem was already detected by Goda (2010) and Suh and Dalrymple (1993), and thus, finer discretization of the input energy spectra was recommended. Increasing the number of frequency bins might decrease the alongshore wave height variation. However, this is due to the decreased energy of each frequency bin which contains a few coherent waves. Therefore, the interference of coherent waves with lower energy levels could result in a more uniform wave height distribution over the domain. Nonetheless, coherent waves are still present in the domain and can manipulate nearshore wave processes.

It is unclear how this method of spectrum discretization affected the results in the previous studies on the nearshore wave processes using the Boussinesq-type models like FUNWAVE-TVD. For example, J. Choi

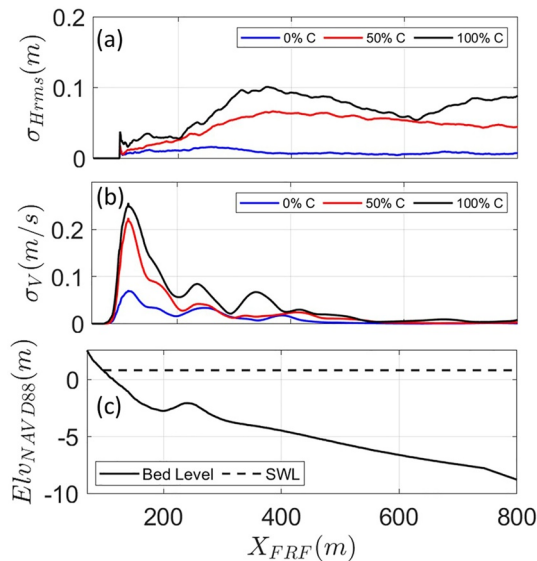


**Figure 12.** Longshore standard deviations of (a)  $H_{rms}$  and (b) longshore currents for three different levels of wave coherence, as well as (c) cross-shore transect of bottom elevation and still water level.

et al. (2015) used the default wavemaker to simulate the SandyDuck experiment. Given the longshore non-uniformity of the bottom topography, longshore variations in the nearshore currents and wave height could be a mixed result of varying topography and input spectrum. A similar potential issue could be found in Y. Choi et al. (2019) for wave height prediction near a port. Chen et al. (2003) simulated the DELILAH experiment (Birkemeier et al., 1997) with directional waves of large incident angle (mean wave direction of  $-35^\circ$  with respect to shore normal). Though they obtained good estimates of the nearshore currents in agreement with the field measurements, we have learned from preliminary simulations using the new wavemaker that increasing the angle of wave incidence reduces the effect of the wave coherence on the alongshore currents. In another study, Feddersen et al. (2011) used the same discretization method of G. Wei et al. (1999) in funwaveC. Despite overall good agreement of the simulation results with the field observations, the effect of wave coherence is masked by alongshore variations in topography. While the authors attributed discrepancies between model and data to bathymetric uncertainties as a factor, wave coherence generated by the default wavemaker could also play a role.

Like nearshore currents, wave runup could also be affected by wave coherence in former studies. However, most of the literature on wave runup simulations based on Boussinesq equations are either in 1D or with regular and solitary waves (Chen et al., 2000; Fuhrman & Madsen, 2007;

Kennedy et al., 2000; Liang et al., 2013; Tonelli & Petti, 2012). Among the limited 2D studies, Guza and Feddersen (2012) have carried out numerical simulations to determine the effects of wave frequency and directional spread on runup using funwaveC. The source of alongshore variations in their runup results could be traced back to the generation of wave coherence by the default wavemaker. The new wavemaker introduced in this study provides a tool to separate the effects of wave coherence on alongshore variability of nearshore wave processes from topographic effects.

To imitate the real-world conditions, some assumptions could be made. For instance, in an analytic wave energy spectrum, some wave frequencies might have coherent waves. Moreover, the wave energy in each component of the coherent waves could also be random. The proposed wavemaker satisfies some of the previously stated assumptions like the randomness of the frequencies, though their energy levels still follow the directional weight of each wave angle determined by Equation 7. However, a thorough analysis of the offshore wave data would be helpful to obtain a robust understanding of wave coherence including their source and energy proportions within the wave energy spectra.

In this section, the effects of the limited number of coherent waves on the nearshore wave processes are assessed and discussed. For this purpose, the longshore averaged topography of the FRF, Duck, NC is utilized with the model setup like the previous section except this time waves are propagating with a mean direction of normally incident to the shoreline. Furthermore, from the 1,550 original wave components with unique frequencies generated by the new wavemaker in the absence of wave coherence, 50% of the wave components form groups of coherent waves by being displaced from their original frequencies. Therefore, some wave frequencies accommodate several wave components propagating in different directions.

The effects of the limited number of coherent waves on some selected nearshore wave processes are demonstrated with the standard deviations of the  $H_{rms}$  and longshore mean current field in Figure 12. With an increase in the wave coherence from 0% to 50% and then to 100%, both the  $H_{rms}$  and  $V$  demonstrate a significant increase in longshore variations. Moreover, wave breaking over the sandbar decreases the longshore variation of the wave height, though its effect on the longshore currents is opposite. This is due to the formation of the large rip currents with the increasing levels of the wave coherence for the normally incident cases as illustrated in Figure 13j–13l. Furthermore, larger variations of the longshore currents can be misleading in estimating the maximum longshore currents from the field measurements since it might be a mixed effect of the bathymetric features and high levels of wave coherence.

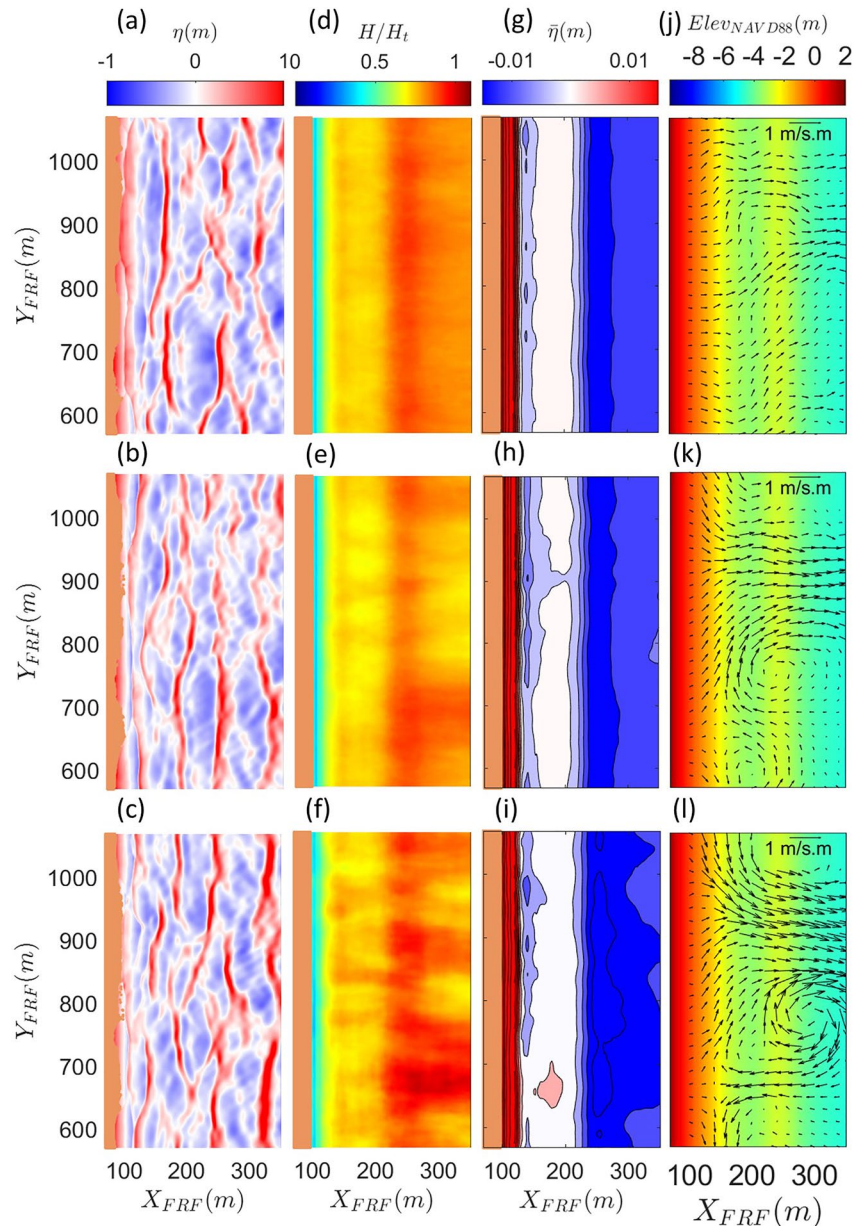


**Figure 13.** Spatial distributions of (a–c) instantaneous surface elevation, (d–f) nondimensionalized  $H_{rms}$ , (g–i) mean water level, and (j–l) depth-integrated mean current field for spectra with 0%, 50%, and 100% wave coherence, respectively.

Figure 13 demonstrates the spatial distribution of the nondimensionalized root mean square wave height, mean current field, and mean water level for the case with the normally incident waves and three levels of wave coherence. Formation of rip currents due to the wave coherence in nodal regions can be observed from the panels (d–f) of Figure 13. It is interesting to note that the wave incidence angle plays an important role in the intensity of the mean current field variations due to the wave coherence. As shown in Figure 13, in the normally incident wave cases, the wave coherence results in the formation of strong rip currents in the domain. However, in more oblique cases, like Chen et al. (2003), the stronger longshore currents have been observed to suppress the rip currents and result in a more uniform mean current field, as demonstrated in Figure 10. Furthermore, for a normally incident case using the default directional wavemaker of FUNWAVE TVD, all wave components in a discretized wave energy spectrum are symmetric and thus, one would expect a similar mean current field of the case with two identical regular waves forming a rip current



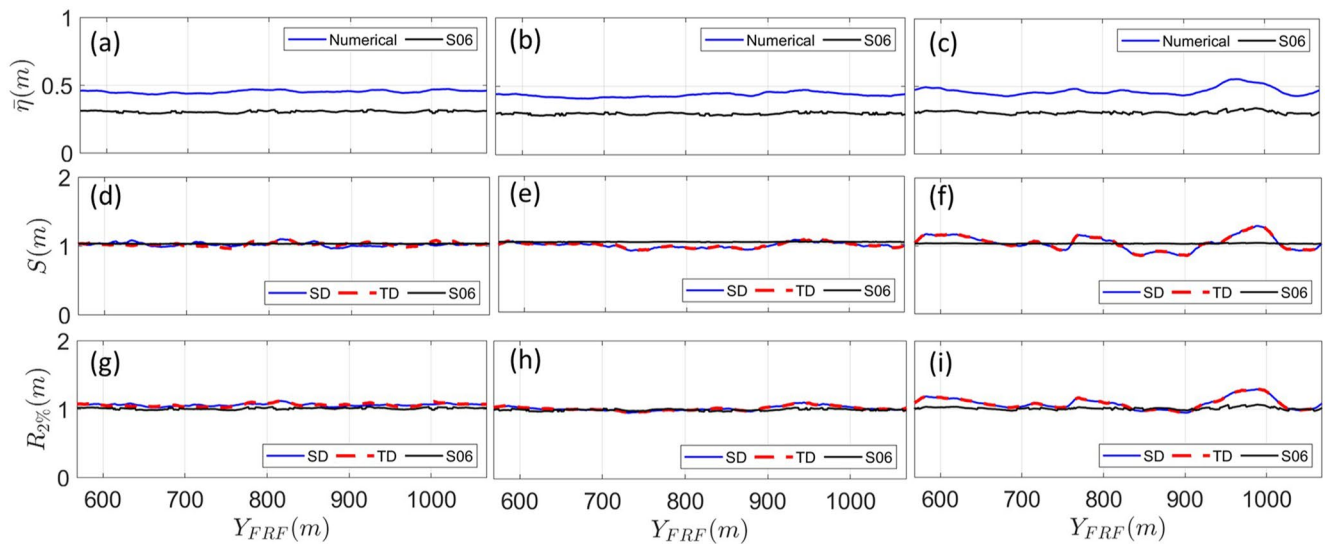


**Figure 14.** (a–c) Wave setup, (d–f) significant swash height, and (g–i) extreme wave runup,  $R_{2\%}$ , for the normally incident case for spectra with 0%, 50%, and 100% wave coherence, respectively.

at the middle of the domain as in J. Choi and Roh (2021). However, the addition of the random phases to the wave components displaces the nodal and anti-nodal regions and consequently, moves the stationary rip current to new random locations, further complicating the analyses of nearshore hydrodynamics in presence of coherent waves. In the current study, since all scenarios are analyzed with the same machine, the pseudo-random phase numbers are the same for all cases and the results are not affected by the new random phase numbers for wave components.

Wave setup and extreme wave runup are also illustrated in Figure 14. Longshore variations in the wave setup can be attributed to wave coherence, which consequently affects the extreme wave runup values. However, wave runup is mainly affected by the infra-gravity wave signals, as illustrated in Figures 11g and 11h. Similar to the obliquely incident case, the setup values by the numerical experiments are higher than the empirical values by Stockdon et al. (2006) for the normally incident case. However, in cases with no wave coherence, the numerical experiments coincide with the empirical values of the extreme wave runup. The difference in empirical and numerical values of wave setup and wave runup can be due to the directional and frequency spreading of the energy spectra (Feddersen, 2004; O'Dea & Haller, 2015) since these parameters are not considered by Stockdon et al. (2006). Additionally, for the significant swash height and extreme runup, both time domain and spectral domain analysis methods result in the same values, indicating that these methods give the same results in the absence of alongshore bathymetric variations.

Effects of the wave coherence on the wave setup and extreme wave runup values are important, because of their effects on the morphological changes (Dalrymple & Lanan, 1976). Moreover, wave setup and runup can also be used as efficient measures of wave coherence in field experiments when using an array of wave gauges for the wave coherence recording seems impractical (Smit et al., 2016). Overall, wave coherence can potentially affect many nearshore processes and can deviate them from the analytical solutions. Therefore, in the absence of enough information on the level of wave coherence in offshore wave energy spectra, a degree of uncertainty in the nearshore wave processes due to the potential presence of coherent waves should be considered. Thus, analyses of the wavefield with varying degrees of wave coherence could assist one in estimating the level of wave coherence in the real world and better simulate the nearshore hydrodynamics.

## 6. Conclusions

Coherent waves are thought to affect many nearshore wave processes. These interfering waves result in nodal and anti-nodal regions throughout the domain because of their relative phase difference and consequently, lead to longshore variations in wave height and mean water level. The change in mean water level,

as well as the excess momentum due to the abrupt wave height variations throughout the domain, complicates many nearshore wave processes. Here, we have developed a new directional wavemaker which either eliminates or limits the number of coherent waves generated by the wavemaker. Then, using the default and new wavemaker, we can probe the effects of the coherent waves on the nearshore wave processes.

In the current study, we performed two sets of numerical experiments. The first set was a flat bottom case, where we aimed to investigate the wave height variations due to the coherent waves in the absence of any morphological effects. We showed that coherent waves result in longshore and cross-shore varying wave height distributions over the domain. However, the shape of the input spectrum determines the wave height variation intensity. Moreover, cross-shore and longshore transects of the wave height demonstrated that the new wavemaker can generate the target wave height at the wavemaker location. The surface elevation data obtained from the wave gauges in the modeled wavefield revealed that the new wavemaker can regenerate the input directional wave energy spectra throughout the domain. For the default wavemaker, since the nodal and anti-nodal points of the waves with different frequencies vary spatially, the wave energy spectra demonstrated some frequencies with higher energy compared to the adjacent frequencies, which are different from the input spectra.

The second set was the longshore averaged bathymetry of the Field Research Facility at Duck, NC. A set of numerical experiments with obliquely incident waves were carried out using the default as well as the newly developed wavemaker (with zero wave coherence). In addition to the longshore varying wave height, variations in mean water level were also observed. The anti-nodal regions having larger wave height also had relatively lower water levels. In the absence of the coherent waves, the mean current field was longshore uniform with no shear instabilities occurring near the shoreline. However, in anti-nodal regions using the default wavemaker, shear instabilities were observed at these regions with the generation of rip currents. Shear wave amplitudes were also shown to increase while approaching the shoreline. Then, the runup time series were obtained and analyzed both in time and frequency domains and the setup and extreme runup values ( $R_{2\%}$ ) were compared to the values obtained by empirical equations. It was found out that the setup values were larger compared to the empirical values. Though no good agreement was found between the numerical and empirical setup values, the  $R_{2\%}$  values for both methods better correlated for the new wavemaker. Furthermore, though the longshore variations of wave setup and  $R_{2\%}$  were higher in the cases with the default wavemaker, small longshore variations could also be observed in cases with no coherent waves. We showed that the longshore variation of the wave runup is only partly due to the wave coherence, and nonlinear wave-wave interactions and infragravity wave signals drive some of the longshore wave runup non-uniformity in both wavemakers.

Lastly, increasing levels of wave coherence in the normally incident waves were also investigated for the FRF domain in the discussion. It was shown that an intermediate level of coherence results in similar longshore patterns in the processes outlined above. However, their intensity is lower than the fully coherent wavefield. Since our understanding of wave coherence in real-world conditions is limited, varying levels of wave coherence implemented in the new wavemaker can help the community to reach a better understanding of the effects of wave coherence with the numerical models and field measurements.

## Appendix A: Default Directional Wavemaker of FUNWAVE-TVD

The time series of the source function for the random waves can be formulated as follows.

$$F(y, t) = \sum_{i=1}^N \sum_{j=1}^M D_{ij} \cos(\omega_i t - k_i \cos(\theta_j) y + \phi_{ij}), \quad (\text{A1})$$

where subscripts  $i$  and  $j$  correspond to the frequency and directional components, and  $\omega_i$ ,  $k_i$ ,  $\theta_j$  are the phase speed, wave number, and wave direction for each frequency component, respectively. Additionally,  $\phi_{ij}$  is a random phase with values in the range of  $[0, 2\pi]$  and  $D_{ij}$  is the amplitude of the source function for each wave component as follows.

$$D_{ij} = \frac{2a_{ij}(\omega_i^2 - \alpha_1 g k_i^4 h^3) \cos(\theta_j)}{\omega_i I_1 k_i (1 - \alpha k_i^2 h^2)}, \quad (\text{A2})$$

in which  $a_{ij}$  is the wave amplitude of each wave component and  $I_1$  is a parameter determined as follows

$$I_1 = \sqrt{\frac{\pi}{\beta_i}} e^{-\frac{k_i^2 \cos^2(\theta_j)}{4\beta_i}}. \quad (\text{A3})$$

Since the input energy spectrum is divided into a certain number of frequency and directional components, the wave amplitude corresponding to each component is calculated as follows

$$a_{ij} = \sqrt{\frac{E_i \bar{A}_j H_{mo}^2 df}{8 \Sigma_i E_i df}}, \quad (\text{A4})$$

where  $H_{mo}$  is the target significant wave height,  $E_i$  is the energy density of each frequency component based on the discretized TMA spectrum and  $A_j$  is the directional weight of each directional component. The TMA spectrum for the energy density of each frequency component can be formulated as follows

$$E_i = \phi_i g^2 f_i^{-5} (2\pi)^{-4} \gamma_{TMA}^{Z_i} \exp\left(-\frac{5}{4} \left(\frac{f_i}{f_p}\right)^4\right), \quad (\text{A5})$$

where  $\phi_i$  is a frequency dependent factor which transforms the deep-water formulation to the finite depth equivalent and is determined as follows

$$\phi_i(2\pi f, h) = \begin{cases} \frac{\omega_i^2}{2} & \text{for } \omega_i \leq 1 \\ 1 - \frac{(2 - \omega_i)^2}{2} & \text{for } 1 < \omega_i < 2 \\ 1 & \text{for } \omega_i \geq 2 \end{cases} \quad (\text{A6})$$

and  $\omega_i$  is

$$\omega_i = 2\pi f_i \sqrt{\frac{h}{g}}. \quad (\text{A7})$$

Moreover,  $Z_i$  is

$$Z_i = \exp\left(\left(\frac{f_i}{f_p} - 1\right)^2 / (-2\sigma^2)\right), \quad (\text{A8})$$

where  $\sigma$  for the frequency range above and below the peak frequency can be determined as

$$\sigma = \begin{cases} 0.09 & \text{for } f_i > f_p \\ 0.07 & \text{for } f_i \leq f_p \end{cases}. \quad (\text{A9})$$

The directional weight  $A_j$  for each of the directional bins is also determined as

$$A_j = \frac{1}{2\pi} + \frac{1}{\pi} \sum_{k_n=1}^{N_s} \left( e^{-0.5(k_n^* \sigma_\theta)^2} \right) \cos(k_n^* (\theta_j - \theta_{\text{mean}})) \quad (\text{A10})$$

where  $N_s$  is defined as

$$N_s = 20/\sigma_\theta \quad (\text{A11})$$

and  $\sigma_\theta$  is the directional spreading parameter. Furthermore,  $\theta_j$  and  $\theta_{\text{mean}}$  are the wave component direction and the mean propagation direction angle, respectively. The directional weight, however, is normalized in the directional axis as

$$\bar{A}_j = \frac{A_j}{\Sigma_j A_j}. \quad (\text{A12})$$

Thus, the integration of the directional weight over a frequency component is always equal to one.

## Appendix B: Empirical Equations for Wave Setup and $R_{2\%}$

According to Stockdon et al. (2006), the  $R_{2\%}$  can be determined as follows

$$R_{2\%} = 1.1 \left[ \bar{\eta} + \frac{S}{2} \right] \quad (\text{B1})$$

where  $\bar{\eta}$  and  $S$  denote the wave setup and significant swash height, respectively. Wave setup is simply obtained by averaging the runup values over a specified time. In spectral-domain analyses, significant swash height can be expressed as four times the square root of the area under the power spectral density of runup.

$$S_s = 4 \sqrt{\sum \text{PSD}(f) * df} \quad (\text{B2})$$

In time-domain analyses, this value is attained by four times the standard deviation of the runup values.

$$S_t = 4 \text{std}(\eta) \quad (\text{B3})$$

Though the extreme runup values can be obtained through the aforementioned methods with the presence of the runup data for a sufficient period, the empirical equations developed by Stockdon et al. (2006) can also be a guideline in obtaining the extreme runup values when runup data is not present. Stockdon et al. (2006) provide two empirical equations, one of which is used for extremely dissipative beaches and the other is used for natural beaches. The beach type is determined by the Iribarren number which can be defined as the dynamic beach steepness and is formulated as follows

$$\xi_0 = \frac{\beta_f}{\sqrt{H_0/L_0}} \quad (\text{B4})$$

with the  $\beta_f$  as the foreshore beach slope,  $H_0$  as the deep-water wave height, and  $L_0$  as the deep-water wavelength. The Iribarren number for natural and extremely dissipative beaches is  $\xi_0 \geq 0.3$  and  $\xi_0 < 0.3$ , respectively. The FRF domain can be included within the category of natural beaches. For the natural beaches, the setup can be determined as follows

$$\bar{\eta} = 0.35 \beta_f \sqrt{H_0 L_0}. \quad (\text{B5})$$

And the significant incident and infragravity swash heights can be determined according to the following equations

$$S_{\text{in}} = 0.75 \beta_f \sqrt{H_0 L_0}, \quad (\text{B6})$$

$$S_{\text{ig}} = 0.06 \sqrt{H_0 L_0}. \quad (\text{B7})$$

It should be noted that  $f = 0.05$  Hz is considered as the threshold for decomposing the frequency band into the incident and infragravity bands, and the total significant swash height is calculated according to Equation B8.

$$S = \sqrt{S_{\text{in}}^2 + S_{\text{ig}}^2} \quad (\text{B8})$$

Substituting the Equations B5–B7 in Equation B1 results in a general equation for the extreme runup for natural beaches as follows

$$R_{2\%} = 1.1 \left( 0.35 \beta_f \sqrt{H_0 L_0} + \frac{\left[ H_0 L_0 (0.563 \beta_f^2 + 0.004) \right]^{\frac{1}{2}}}{2} \right) \quad (\text{B9})$$

while for extremely dissipative beaches, the equation is much simpler and only depends on the offshore wave height and wavelength without dependence on the foreshore beach slope as illustrated in Equation B10.

$$R_{2\%} = 0.043 \sqrt{H_0 L_0} \quad (\text{B10})$$



According to Stockdon et al. (2006), the foreshore beach slope is defined as the average slope of an area covering 2 standard deviations of the continuous water level record around the mean water level. To determine this value for each cross-shore transect, the water level records of the numerical experiments can be utilized.

## Data Availability Statement

The FRF 8m Array data is available at <https://chlthredds.erdc.dren.mil/thredds/catalog/frf/oceanography/waves/8m-array/catalog.html>. The FRF CRAB data is available at <https://chlthredds.erdc.dren.mil/thredds/catalog/frf/geomorphology/elevationTransects/survey/data/catalog.html>.

## Acknowledgments

The research has been supported by the National Science Foundation (NSF) Cyber SEES program (NSF grant number 1856359).

## References

- Akrish, G., Smit, P., Zijlema, M., & Reniers, A. (2020). Modelling statistical wave interferences over shear currents. *Journal of Fluid Mechanics*, 891, A2. <https://doi.org/10.1017/jfm.2020.143>
- Birkemeier, W., Donoghue, C., Long, C., Hathaway, K., & Baron, C. F. (1997). DELILAH nearshore experiment: Summary report. *US Army Engineer Waterways Experiment Station, CHL-97-24*, 1–217.
- Chawla, A., & Kirby, J. T. (2000). A source function method for generation of waves on currents in Boussinesq models. *Applied Ocean Research*, 22(2), 75–83. [https://doi.org/10.1016/S0141-1187\(00\)00005-5](https://doi.org/10.1016/S0141-1187(00)00005-5)
- Chen, Q. (2006). Fully nonlinear Boussinesq-type equations for waves and currents over porous beds. *Journal of Engineering Mechanics*, 132(2), 220–230. [https://doi.org/10.1061/\(asce\)0733-9399\(2006\)132:2\(220\)](https://doi.org/10.1061/(asce)0733-9399(2006)132:2(220))
- Chen, Q., Dalrymple, R. A., Kirby, J. T., Kennedy, A. B., & Haller, M. C. (1999). Boussinesq modeling of a rip current system. *Journal of Geophysical Research*, 104(C9), 20617–20637. <https://doi.org/10.1029/1999jc900154>
- Chen, Q., Kirby, J. T., Dalrymple, R. A., Kennedy, A. B., & Chawla, A. (2000). Boussinesq modeling of wave transformation, breaking, and runup. II: 2D. *Journal of Waterway, Port, Coastal, and Ocean Engineering*, 126(1), 48–56. [https://doi.org/10.1061/\(asce\)0733-950x\(2000\)126:1\(48\)](https://doi.org/10.1061/(asce)0733-950x(2000)126:1(48))
- Chen, Q., Kirby, J. T., Dalrymple, R. A., Shi, F., & Thornton, E. B. (2003). Boussinesq modeling of longshore currents. *Journal of Geophysical Research*, 108(11), 1–18. <https://doi.org/10.1029/2002JC001308>
- Chen, Q., Madsen, P. A., & Basco, D. R. (1999). Current effects on nonlinear interactions of shallow-water waves. *Journal of Waterway, Port, Coastal, and Ocean Engineering*, 125(4), 1764–1786. [https://doi.org/10.1061/\(asce\)0733-950x\(1999\)125:4\(176\)](https://doi.org/10.1061/(asce)0733-950x(1999)125:4(176))
- Choi, J., Kirby, J. T., & Yoon, S. B. (2015). Boussinesq modeling of longshore currents in the SandyDuck experiment under directional random wave conditions. *Coastal Engineering*, 101, 17–34. <https://doi.org/10.1016/j.coastaleng.2015.04.005>
- Choi, J., Lim, C. H., Lee, J. I., & Yoon, S. B. (2009). Evolution of waves and currents over a submerged laboratory shoal. *Coastal Engineering*, 56(3), 297–312. <https://doi.org/10.1016/j.coastaleng.2008.09.002>
- Choi, J., & Roh, M. (2021). A laboratory experiment of rip currents between the ends of breaking wave crests. *Coastal Engineering*, 164, 103812. <https://doi.org/10.1016/j.coastaleng.2020.103812>
- Choi, Y., Seo, S., Choi, J., Shi, F., & Park, K. (2019). Wave prediction in a port using a fully nonlinear Boussinesq. *Acta Oceanologica Sinica*, 38(7), 36–47. <https://doi.org/10.1007/s13131-019-1456-2>
- Choi, Y. K., Shi, F., Malej, M., & Smith, J. M. (2018). Performance of various shock-capturing-type reconstruction schemes in the Boussinesq wave model, FUNWAVE-TVD. *Ocean Modelling*, 131, 86–100. <https://doi.org/10.1016/j.ocemod.2018.09.004>
- Dalrymple, R. A. (1975). A mechanism for rip current generation on an open coast. *Journal of Geophysical Research*, 80(24), 3485–3487. <https://doi.org/10.1029/JC080i024p03485>
- Dalrymple, R. A., & Lanang, G. A. (1976). Beach cusps formed by intersecting waves. *GSA Bulletin*, 87(1), 572–660. [https://doi.org/10.1130/0016-7606\(1976\)87<57:bcfbw>2.0.co;2](https://doi.org/10.1130/0016-7606(1976)87<57:bcfbw>2.0.co;2)
- Feddersen, F. (2004). Effect of wave directional spread on the radiation stress: Comparing theory and observations. *Coastal Engineering*, 51(5–6), 473–481. <https://doi.org/10.1016/j.coastaleng.2004.05.008>
- Feddersen, F., Clark, D. B., & Guza, R. T. (2011). Modeling surf zone tracer plumes: 1. Waves, mean currents, and low-frequency eddies. *Journal of Geophysical Research*, 116(C11), C11027. <https://doi.org/10.1029/2011JC007210>
- Fuhrman, D. R., & Madsen, P. A. (2007). Simulation of nonlinear wave run-up with a high-order Boussinesq model. *Coastal Engineering*, 55, 139–154. <https://doi.org/10.1016/j.coastaleng.2007.09.006>
- Gobbi, M. F., Kirby, J. T., & Wei, G. (2000). A fully nonlinear Boussinesq model for surface waves. Part 2. Extension to  $O(kh)^4$ . *Journal of Fluid Mechanics*, 405, 181–210. <https://doi.org/10.1017/S00222112099007247>
- Goda, Y. (2010). *Random seas and design of maritime structures*. World Scientific. <https://doi.org/10.1142/7425>
- Guza, R. T., & Feddersen, F. (2012). Effect of wave frequency and directional spread on shoreline runup. *Geophysical Research Letters*, 39(11), L11607. <https://doi.org/10.1029/2012GL051959>
- Janssen, T. T., Herbers, T. H., & Battjes, J. A. (2008). Evolution of ocean wave statistics in shallow water: Refraction and diffraction over seafloor topography. *Journal of Geophysical Research*, 113(C3), C03024. <https://doi.org/10.1029/2007JC004410>
- Johnson, D. (2002). *DIWASP, a directional wave spectra toolbox for MATLAB®: User manual*. Center for Water Research, The University of Western Australia.
- Johnson, D., & Pattiaratchi, C. (2006). Boussinesq modelling of transient rip currents. *Coastal Engineering*, 53(5–6), 419–439. <https://doi.org/10.1016/j.coastaleng.2005.11.005>
- Karimpour, A., & Chen, Q. (2017). Wind wave analysis in depth limited water using OCEANLYZ, A MATLAB toolbox. *Computers & Geosciences*, 106, 181–189. <https://doi.org/10.1016/j.cageo.2017.06.010>
- Kennedy, A. B., Chen, Q., Kirby, J. T., & Dalrymple, R. A. (2000). Boussinesq modeling of wave transformation, breaking, and runup. I: 1D. *Journal of Waterway, Port, Coastal, and Ocean Engineering*, 126(1), 39–47. [https://doi.org/10.1061/\(asce\)0733-950x\(2000\)126:1\(39\)](https://doi.org/10.1061/(asce)0733-950x(2000)126:1(39))
- Kennedy, A. B., Kirby, J. T., Chen, Q., & Dalrymple, R. A. (2001). Boussinesq-type equations with improved nonlinear performance. *Wave Motion*, 33(3), 225–243. [https://doi.org/10.1016/S0165-2125\(00\)00071-8](https://doi.org/10.1016/S0165-2125(00)00071-8)

- Larsen, J., & Dancy, H. (1983). Open boundaries in short wave simulations—A new approach. *Coastal Engineering*, 7(3), 285–297. [https://doi.org/10.1016/0378-3839\(83\)90022-4](https://doi.org/10.1016/0378-3839(83)90022-4)
- Lerma, A. N., Pedreros, R., Robinet, A., & Senechal, N. (2017). Simulating wave setup and runoff during storm conditions on a complex barred beach. *Coastal Engineering*, 123, 29–41. <https://doi.org/10.1016/j.coastaleng.2017.01.011>
- Liang, D., Gotoh, H., Khayyer, A., & Chen, J. M. (2013). Boussinesq modelling of solitary wave and N-wave runoff on coast. *Applied Ocean Research*, 42, 144–154. <https://doi.org/10.1016/j.apor.2013.05.008>
- Long, C. E., & Oltman-Shay, J. M. (1991). *Directional characteristics of waves in shallow water*. Coastal Engineering Research Center.
- Miles, M. D., & Funke, E. R. (1989). A comparison of methods for synthesis of directional seas. *Journal of Offshore Mechanics and Arctic Engineering*, 111(1), 43–48. <https://doi.org/10.1115/1.3257137>
- O'Dea, A., & Haller, M. C. (2015). Effect of asymmetric directional spreading on the total radiation stress. *Journal of Waterway, Port, Coastal, and Ocean Engineering*, 141(6). [https://doi.org/10.1061/\(asce\)jww.1943-5460.0000302](https://doi.org/10.1061/(asce)jww.1943-5460.0000302)
- Rijnsdorp, D. P., Ruessink, G., & Zijlema, M. (2015). Infragravity-wave dynamics in a barred coastal region, a numerical study. *Journal of Geophysical Research: Oceans*, 120(6), 4068–4089. <https://doi.org/10.1002/2014JC010450>
- Shi, F., Kirby, J. T., Harris, J. C., Geiman, J. D., & Grilli, S. T. (2012). A high-order adaptive time-stepping TVD solver for Boussinesq modeling of breaking waves and coastal inundation. *Ocean Modelling*, 43–44, 36–51. <https://doi.org/10.1016/j.ocemod.2011.12.004>
- Smit, P. B., Bland, R., Janssen, T. T., & Laughlin, B. (2016). Remote sensing of nearshore wave interference. *Journal of Geophysical Research: Oceans*, 121(5), 3409–3421. <https://doi.org/10.1002/2016JC011705>
- Smit, P. B., & Janssen, T. T. (2013). The evolution of inhomogeneous wave statistics through a variable medium. *Journal of Physical Oceanography*, 43(8), 1741–1758. <https://doi.org/10.1175/JPO-D-13-046.1>
- Smit, P. B., & Janssen, T. T. (2016). The evolution of nonlinear wave statistics through a variable medium. *Journal of Physical Oceanography*, 46(2), 621–634. <https://doi.org/10.1175/JPO-D-15-0146.1>
- Smit, P. B., Janssen, T. T., & Herbers, T. H. (2015a). Stochastic modeling of coherent wave fields over variable depth. *Journal of Physical Oceanography*, 45(4), 1139–1154. <https://doi.org/10.1175/JPO-D-14-0219.1>
- Smit, P. B., Janssen, T. T., & Herbers, T. H. (2015b). Stochastic modeling of inhomogeneous ocean waves. *Ocean Modelling*, 96(1), 26–35. <https://doi.org/10.1016/j.ocemod.2015.06.009>
- Stockdon, H. F., Holman, R. A., Howd, P. A., & Sallenger, A. H., Jr. (2006). Empirical parameterization of setup, swash, and runoff. *Coastal Engineering*, 53(7), 573–588. <https://doi.org/10.1016/j.coastaleng.2005.12.005>
- Suanda, S. H., & Feddersen, F. (2015). A self-similar scaling for cross-shelf exchange driven by transient rip currents. *Geophysical Research Letters*, 42(13), 5427–5434. <https://doi.org/10.1002/2015GL063944>
- Suh, K. D., & Dalrymple, R. A. (1993). Application of angular spectrum model to simulation of irregular wave propagation. *Journal of Waterway, Port, Coastal, and Ocean Engineering*, 119(5), 505–520. [https://doi.org/10.1061/\(asce\)0733-950x\(1993\)119:5\(505\)](https://doi.org/10.1061/(asce)0733-950x(1993)119:5(505))
- Tonelli, M., & Petti, M. (2012). Shock-capturing Boussinesq model for irregular wave propagation. *Coastal Engineering*, 61, 8–19. <https://doi.org/10.1016/j.coastaleng.2011.11.006>
- Van Dongeren, A., Reniers, A., Battjes, J., & Svendsen, I. (2003). Numerical modeling of infragravity wave response during DELILAH. *Journal of Geophysical Research*, 108(C9), 3288. <https://doi.org/10.1029/2002JC001332>
- Wei, G., Kirby, J. T., & Sinha, A. (1999). Generation of waves in Boussinesq models using a source function method. *Coastal Engineering*, 36(4), 271–299. [https://doi.org/10.1016/S0378-3839\(99\)00009-5](https://doi.org/10.1016/S0378-3839(99)00009-5)
- Wei, Z., & Dalrymple, R. A. (2017). SPH modeling of vorticity generation by short-crested wave breaking. *Coastal Engineering Proceedings*, 1(35), 1. <https://doi.org/10.9753/icce.v35.waves.1>
- Young, T. (1802). *On the theory of light and colours*. Royal Society of London.